Biocatalytic mechanistic investigation of sulfur oxidation in dimeric model of polyphenylene sulfide polymer (PPS) by DszC enzyme

Pei Wang, Changru Ma, Anthony Bocahut, Sophie Sacquin-Mora, Carine Michel, Natacha Gillet

2 December 2025

Biocatalytic Mechanistic Investigation of Sulfur Oxidation in Dimeric Model of Polyphenylene Sulfide Polymer (PPS) by DszC Enzyme

Pei Wang[2,1], Changru Ma[3], Anthony Bocahut[4], Sophie Sacquin-Mora[5], Carine Michel[1], Natacha Gillet[1]

1. CNRS, ENS de Lyon, Laboratoire de Chimie, UMR 5182, 46 Allée d'Italie, F-69342 Lyon, France

2. College of Chemistry, Huazhong Agricultural University, Wuhan 430070, PR China

3. Eco-Efficient Products and Processes Laboratory (E2P2L), UMI 3464/CNRS-Syensqo, 3966 Jindu Road, Xin Zhuang Industrial Zone, Shanghai 201108, China

4. Syensqo Specialty Polymers, Bâtiment Axel'One, 87 avenue des Frères Perret, 69192 Saint-Fons, France

5. Université Paris Cité, CNRS, Laboratoire de Biochimie Théorique, UPR9080, 13 rue Pierre et Marie Curie, F-75005, Paris, France

Abstract

Polyphenylene sulfide (PPS) is a sulfur-containing polymer widely used in high-performance materials. Its stability makes PPS challenging to recycle. Herein, we report a computational study of the catalysis of the oxidation of dimeric PPS (DPS) to its sulfoxide derivative (DPSO) by DszC, a flavin-dependent monooxygenase from the 4S pathway. Molecular dynamics (MD) simulations reveal that DPS preferentially localizes near the flavin C4a-hydroperoxide intermediate within DszC's hydrophobic cavity. Analysis of hydrogen-bond networks involving the C4a-hydroperoxide hydrogen and oxygen atoms highlighted five distinct starting structures for hybrid QM/MM Nudged Elastic Band calculations involving intramolecular stabilization with the D-ribitol tail, intermolecular contacts with His391 and Tyr96, and two water-mediated networks. Free energy barrier analysis demonstrated that enhanced stabilization of the proximal oxygen of the flavin C4a-hydroperoxide lowers the proximal O-O bond cleavage barrier. Indeed, the lowest barrier is observed when both His391 and Tyr96 residues are involved in the hydrogen bond network with the reactant. Moreover, a water molecule also stabilizes the transition state via hydrogen bonding with the distal oxygen, yielding a comparable barrier. These findings suggest that enzymatic DPS oxidation by DszC protein is feasible, opening the way of new biodegradation pathway of PPS polymers.

https://doi.org/10.26434/chemrxiv-2025-ds9mk

Keywords

Oxidative desulfurization, Flavin-dependent monooxygenase, Polyphenylene sulfide (PPS), molecular dynamics, quantum mechanics/molecular mechanics

Biocatalytic Mechanistic Investigation of Sulfur Oxidation in Dimeric Model of Polyphenylene Sulfide Polymer (PPS) by DszC Enzyme

Pei Wang[a,b], Changru Ma[c], Anthony Bocahut[d], Sophie Sacquin-Mora[e], Carine Michel[a], Natacha Gillet[a]

a CNRS, ENS de Lyon, Laboratoire de Chimie, UMR 5182, 46 Allée d'Italie, F-69342 Lyon, France

b College of Chemistry, Huazhong Agricultural University, Wuhan 430070, PR China

c Eco-Efficient Products and Processes Laboratory (E2P2L), UMI 3464/CNRS-Syensqo, 3966 Jindu Road, Xin Zhuang Industrial Zone, Shanghai 201108, China

d Syensqo Specialty Polymers, Bâtiment Axel'One, 87 avenue des Frères Perret, 69192 Saint-Fons, France

e Université Paris Cité, CNRS, Laboratoire de Biochimie Théorique, UPR9080, 13 rue Pierre et Marie Curie, F-75005, Paris, France

natacha.gillet@ens-lyon.fr

Abstract

Polyphenylene sulfide (PPS) is a sulfur-containing polymer widely used in high-performance materials. Its stability makes PPS challenging to recycle. Herein, we report a computational study of the catalysis of the oxidation of dimeric PPS (DPS) to its sulfoxide derivative (DPSO) by DszC, a flavin-dependent monooxygenase from the 4S pathway. Molecular dynamics (MD) simulations reveal that DPS preferentially localizes near the flavin C^{4a}-hydroperoxide intermediate within DszC's hydrophobic cavity. Analysis of hydrogen-bond networks involving the C^{4a}-hydroperoxide hydrogen and oxygen atoms highlighted five distinct starting structures for hybrid QM/MM Nudged Elastic Band calculations involving intramolecular stabilization with the D-ribitol tail, intermolecular contacts with His391 and Tyr96, and two water-mediated networks. Free energy barrier analysis demonstrated that enhanced stabilization of the proximal oxygen of the flavin C^{4a}-hydroperoxide lowers the proximal O-O bond cleavage barrier. Indeed, the lowest barrier is observed when both His391 and Tyr96 residues are involved in the hydrogen bond

network with the reactant. Moreover, a water molecule also stabilizes the transition state via hydrogen bonding with the distal oxygen, yielding a comparable barrier. These findings suggest that enzymatic DPS oxidation by DszC protein is feasible, opening the way of new biodegradation pathway of PPS polymers.

Key words

Oxidative desulfurization, C-S bond, Flavin-dependent monooxygenase, Polyphenylene sulfide (PPS), molecular dynamics, quantum mechanics/molecular mechanics

1. Introduction

Polyphenylene sulfide (PPS) is a high-performance engineering thermoplastic renowned for its exceptional thermal stability and chemical resistance for applications across the aerospace, electronics, and automotive sectors [1,2,3,4,5]. This industrial significance is underscored by market data: the global PPS market reached USD 1305.34 million in 2024 and is projected to grow at a compound annual growth rate (CAGR) of 8.3% from 2024 to 2031 [6,7] . However, the escalating production demand exacerbates a critical issue in term of sustainability —while PPS delivers superior material performance [6,7], its sulfur-rich backbone (30–35 wt%) poses substantial challenges for the thermal recycling since thermal processing of PPS releases carcinogenic sulfur oxides, creating significant health and ecological hazards [8,9].

One sustainable way could be inspired by the biodegradation of the carbon-backbone polymers such as polyethylene terephthalate (PET). Indeed, PET biodegradation pathways targeting ester or aliphatic linkages are now well-characterized and even engineered for industrial application [10,11,12,13,14,15]. Microbial desulfurization has emerged as a promising alternative for surlfur-containing polymers, offering harmless treatment under mild reaction conditions [16,17,18]. Recent studies have demonstrated that *Pseudomonas* bacteria can achieve partial PPS degradation, albeit only over extended incubation periods (30–60 days) [19,20]. Three fundamental knowledge gaps currently hinder progress in this field: (1) the lack

of identified desulfurases capable of cleaving polymeric C-S bonds, (2) the undefined molecular mechanisms governing enzymatic desulfurization processes, and (3) limited understanding of enzyme-macromolecule interface interactions. Innovative strategies integrating computational enzymology and protein engineering can help to overcome these barriers.

A highly interesting model for PPS desulfurization is the 4S pathway, employed by *Rhodococcus* species and related bacteria to degrade dibenzothiophene (DBT)—a process critically important in fossil fuel biodesulfurization [21,22,23,24]. In this pathway, the sequential and coordinated actions of the Dsz enzyme system selectively catalyze the oxidation and cleavage of C–S bonds in DBT, leading to the production of 2-hydroxybiphenyl and inorganic sulfite [21,22,23,24,25,26,27,28,29,30,31]. The process starts with the DszC-catalyzed oxidation of DBT to dibenzothiophene sulfoxide (DBTO), followed by its further oxidation to $DBTO_2$. DszA then catalyzes the first carbon-sulfur bond cleavage of $DBTO_2$ [25,26,27]. Subsequently, DszB cleaves the final C–S bond, yielding 2-hydroxybiphenyl and sulfite [28]. Additionally, DszD facilitates flavin reduction by mediating hydride transfer from NADH, thereby regenerating the reduced flavin cofactor essential for DszC and DszA activity [29]. This well-established mechanistic framework could present an analogy for PPS biodegradation, as both substrates share a central aromatic thioether linkage.

We investigate here an analogous sequence for the enzymatic degradation of PPS using computational models. We hypothesize that PPS undergoes DszC-catalyzed step-wise oxidation to PPS sulfoxide (PPSO) and subsequently to PPS dioxide ($PPSO_2$), followed by DszA/DszB-mediated cleavage of the C–S bonds, ultimately yielding p-hydroxybenzenesulfinate (HBS) and phenol as terminal products (**Figure 1b**). Kinetic analyses of the DBT 4S pathway have identified both the initial DszC-catalyzed oxidation and the final DszB-catalyzed C-S bond cleavage as rate-limiting steps [30]. We focus our study on the first step—DszC-mediated oxidation—as it initiates the catalytic cascade and generates essential intermediates for downstream reactions, using diphenyl sulfide (DPS), the dimeric analog of PPS, as a model of the polymeric substrate.

Since DPS is more flexible than DBT that contains an additional C–C bond bridging the ortho-positions of the two phenyl rings, sampling the conformational

space of the reactant in the catalytic pocket is critical. This will be performed using classical molecular dynamics (MM-MD) to reach a high-quality sampling of the possible orientations of the substrate within the pocket and identify the possible presence of water within the pocket. Besides, the nucleophilicity of the sulfur atom may differ from DBT to DPS. The barrier corresponding to the oxidative attack of the sulfur atom will be carefully investigated using hybrid QM/MM approaches combined with nudge elastic band and transition state optimization. Similar approach was already employed successfully to investigated the DBT oxidation [25]. To tackle the challenge of sampling how conformational changes of the pocket may affect the activity of the catalytic site [32], we will select a variety of starting configurations through careful analysis of the classical molecular dynamics trajectories. Our study, combining both the conformational sampling of DPS in the DszC active pocket and QM/MM evaluation of reaction free energy highlights how DszC active site can adapt to catalyse DPS oxidation.

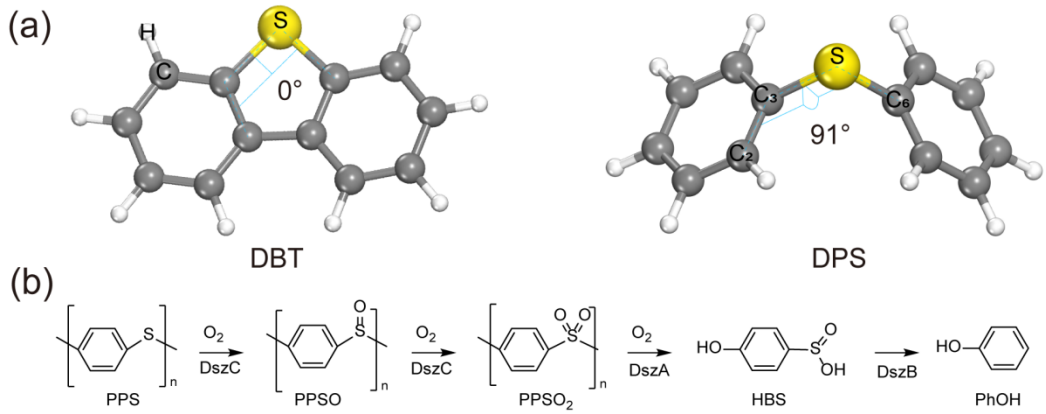

Figure 1. Substrate Structure and Proposed Desulfurization Mechanism. a) Structural comparison of diphenyl sulfide (DPS) and dibenzothiophene (DBT) with sulfur (yellow), hydrogen (white), and carbon (grey) atoms shown as spheres, with inserting the C_2-C_3-S-C_6 dihedral (light blue). b) Proposed enzymatic desulfurization pathway for poly(phenylene sulfide) (PPS) catalyzed by the 4S pathway enzymes DszC, DszA, and DszB.

2. Computational details

Molecular Dynamics Simulations

The FMN-bound DszC structure originates from *Rhodococcus erythropolis* (PDB ID: 3X0Y, resolution 2.3 Å) [33]. A single homodimer (Chain A &F), was selected to represent the DszC enzyme model. This model includes all resolved residues (402 in A, 400 in F) and conserved water molecules. The protonation states of titratable

residues were assigned according to the model described in Barbosa *et al* [25]. Specifically, His92, His388, and His391 in the active site were protonated at the N_δ, while all other histidine residues were protonated at the N_ε [25]. The redox states of flavin (FMN) cofactors were modeled according to their catalytic roles to capture substrate oxidation accurately. In our model (Figure 2), the first monomer features the C^{4a}-hydroperoxyflavin ($C^{4a}OOH$) intermediate directly involved in substrate oxidation, while the second monomer retains reduced FMN ($FMNH^-$) for electronic consistency. The two oxygen of $C^{4a}OOH$ are separately denoted as O_p and O_d, O_p is a proximal oxygen atom, covalently attached to the isoalloxazine ring, and O_d is a distal oxygen that constitutes the reactive terminal atom of the –OOH group (Figure 2). To model polyphenylene sulfide (PPS) reactivity, we used diphenyl sulfide (DPS) as a computationally efficient representative model.

Given the lack of experimental structures for DszC-substrate complexes, we built on the structural similarity between DPS and DBT to construct a DPS:DszC model based on the previously reported DBT:DszC model by Fernandes and coworkers, which using one and half monomer represent DszC model [25,34]. To extend this model to a homodimeric representation, we performed structural superposition using PyMOL align function [35], resulting in initial conformations of the DPS-bound homodimer with alternating redox states ($C^{4a}OOH$ in chain A and $FMNH^-$ in chain F). A similar procedure was employed to construct the DszC-$C^{4a}OOH$:DBT model, the only difference being the distinct structures of DBT and DPS. The initial $S_{DBT\text{-}DPS}$-O_d distance was 3.76 Å, and the $S_{DBT\text{-}DPS}$-O_d-O_p angle was 146.5° degree, coinciding with the DBT:DszC model reported by Barbosa *et al* [25].

All-atom MD simulations were performed using *AMBER20* with the ff14SB force field [36,37,38]. The DBT, C4A and $FMNH^-$ parameters were derived from published quantum mechanical calculations using RESP charges at the B3LYP/6-31G* level [25]. DPS charges and torsion parameters were optimized through HF/6-31G(d,p) calculations using the *TURBOMOLE* software and converted to AMBER force field parameters [39,40]. The $C^{4a}OOH$ was singlet-state based on previous report. The TIP3P water model was used to solvate the complexes [41]. System assembly, solvation, and neutralization were performed using the *tleap* module in *AMBER20*, with 34 Na^+ ions added to neutralize the system. A rectangular water box was constructed, maintaining a minimum distance of 20 Å between the solute and the box boundaries (Figure S1a).

MD simulations were carried out using *AMBER20* for DPS:Dszc and DBT:DszC for comparison. Energy minimization was performed in two stages: 5,000 steps of steepest descent followed by 5,000 steps of conjugate gradient minimization. The system was then gradually heated from 0 K to 300 K over 30 ps in NVT ensemble, employing the Nose-Hoover thermostat with a coupling constant of 1.0 ps^{-1}. Equilibration was conducted for 2 ns under NPT conditions using a 2 fs timestep, with temperature control via the Nose-Hoover thermostat (300 K) and pressure regulation using the Berendsen barostat (1 atm). The production phase consisted of 400 ns using the same parameters. For all simulations, we employed a 10 Å cutoff for nonbonded interactions. Long-range electrostatic interactions were treated with the particle-mesh Ewald (PME) method. The SHAKE algorithm was applied to constrain hydrogen-involving bonds. Trajectory analysis was performed using the *CPPTRAJ* tool to calculate the root-mean-square deviation (RMSD) with reference to the starting PDB structure, root-mean-square fluctuation (RMSF), distance and angular measurements, and radial distribution function (RDF) analysis [42]. The statistical histograms were generated via custom Python scripts.

QM/MM Calculations

QM/MM calculations were conducted to investigate the catalytic mechanism of DPS oxidation using *ORCA* [43,44]. Five representative catalytic conformations were extracted from MD simulations as starting points for QM/MM calculations as detailed in the Results and discussion section.

The system was partitioned into QM and MM regions, as shown in Figure S1. The QM layer was treated with density functional theory (DFT), while the MM layer was described using the FF14SB force field from *AMBER* [38]. The QM layer comprised all atoms of the DPS substrate (23 atoms), the isoalloxazine core and the N^{10}-bound hydroxyethyl of $C^{4a}OOH$ (38 atoms), and side chains of catalytically relevant residues, including His92 (11 atoms), Tyr96 (15 atoms), Asn129 (8 atoms), Ser163 (5 atoms), His388 (11 atoms), and His391(11 atoms) (Figure S1c). Each system contained 122 QM-layer atoms (overall neutral charge, singlet spin state) or 125 QM-layer atoms when an additional water molecule was included, for a total of 168,948 atoms in the simulation box. The link-atom approach was used to maintain valency across QM/MM boundaries, incorporating seven link hydrogen atoms along the C_α-C_β bonds of each amino-acid residue and between the N^{10}-bound hydroxyethyl

and hydropropyl bond of the $C^{4a}OOH$ cofactor. The MM region included all remaining atoms, further subdivided into a frozen region and a flexible region, with residues and waters within 15 Å of the QM layer treated as flexible. An electrostatic embedding was used. The QM region was treated using the B3LYP functional with Grimme's D3BJ dispersion correction and the 6-31G(d,p) basis set.

The initial transition state (TS) structures were identified via the nudged elastic band transition state search (NEB-TS) method, and also followed by full TS optimizations (optTS) to refine the geometries [45,46]. To confirm the nature of each transition state, frequency calculations were conducted, ensuring the presence of one and only one imaginary frequency. For computational efficiency, frequency calculations were performed on a reduced QM region that included only the substrate DPS and the key residues directly involved in the reaction mechanism: $C^{4a}OOH$, Tyr96, and His391, comprising 87 atoms in total. Only vibrational modes with wavenumbers greater than 50 cm^{-1} were considered as harmonic vibrational frequencies. Thermochemical corrections were applied to estimate Gibbs free energies. These corrections incorporated zero-point energy (ZPE) contributions, as well as thermal enthalpy and entropy.

All the structure visualization was conducted using the VMD software [47].

Results and discussion

3. Classical Molecular Dynamics of the DszC:DPS complex

DszC was modeled in its homodimeric form (Figure 2) [25,33], with two catalytic pockets containing a flavin mononucleotide (FMN) cofactor. To oxidize DBT or DPS, the first step is the oxidation of this FMN cofactor into the $C^{4a}OOH$ intermediate. This step is already known as a near-barrierless process [25,48,49]. Consequently, we chose to use a model of the homodimer of DszC with:

(i) one activated site containing the oxidized form of the cofactor, i.e. $C^{4a}OOH$, with O_p the proximal oxygen atom and O_d the distal oxygen that constitutes the reactive terminal atom of the –OOH group (Figure 2). The DPS (or DBT) substrate in close was positioned in proximity to this reactive center (Figure 2) as described previously [25].

(ii) one site containing the reduced form of the cofactor ($FMNH^-$) and no substrate as proposed in previous MD simulations studies of DszC [50].

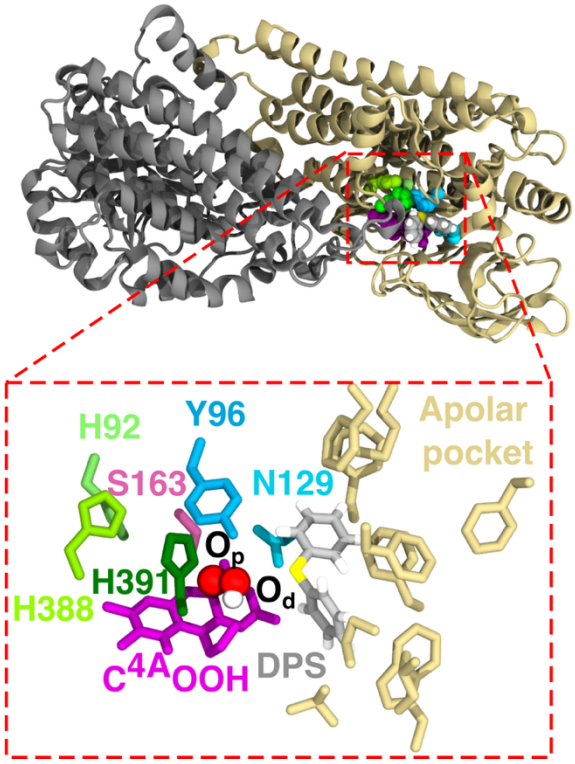

Figure 2. Structure of DszC containing DPS. Cartoon representation of DszC in complex with the $C^{4a}OOH$ cofactor and DPS substrate with an insight to the active site.

Structural and dynamic characterization of DszC:DPS and DszC:DBT

The root-mean-square deviation (RMSD) analysis of the protein backbone confirmed that the DszC homodimer maintains structural stability throughout the 400 ns molecular dynamics simulations, with global RMSD values consistently remaining below 3.0 Å (Figures 3a,b). Residual fluctuations are predominantly localized to flexible loop regions, as further supported by root-mean-square fluctuation (RMSF) profiles and supplementary RMSD analyses (Figures S2–S4). In contrast, the catalytic active site—comprising key residues His92, Tyr96, Asn129, Ser163, His388, and His391, along with the $C^{4a}OOH$ cofactor—exhibited a high structural integrity, underscoring the robustness of the core catalytic architecture. A hydrogen-bonding network formed between these key residues and $C^{4a}OOH$, as well as among these key residues themselves, is observed. This network of interactions mirrors previously reported configurations of DszC [25], and maintains the cofactor in a catalytically active orientation. In more details, the $C^{4a}OOH$ cofactor demonstrates a remarkable stability with RMSD values remaining below 3.0 Å and a mean value of 1.56 Å (Figure 3a,b). Its anchored within the active site through a persistent hydrogen-bonding

network: Tyr96 (phenolic $–O_\eta$ or $O_\eta–H$) and His391 (imidazole $–N_\varepsilon$ or $N_\delta H$) are interacting with the OOH moiety while an additional stabilization is provided by Ser163 (hydroxyl –OH) and Asn129 (amide $–NH_2$), which build hydrogen-bonds with oxygen and nitrogen atoms of the isoalloxazine ring, respectively (Figure S5,S6). These key residues surrounding the co-factor C^{4a}OOH exhibit even smaller structural deviation than this cofactor, with RMSD values remaining below 2.0 Å and a mean value of 1.33 Å (Figure 2b, and Figure S2-S4).

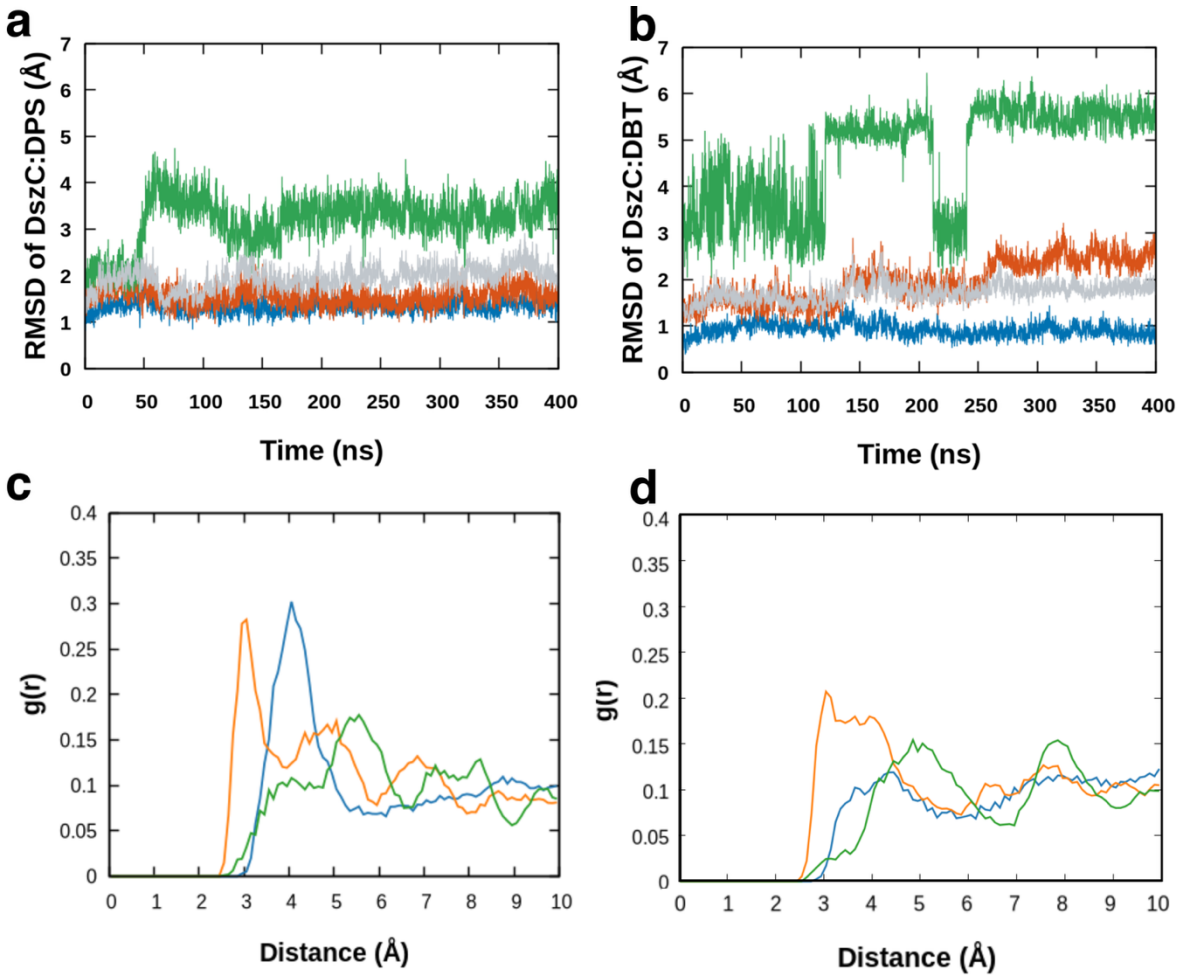

Figure 3. (**a**,**b**)Time evolution of the root-mean-square deviation (RMSD) of DszC's active site (blue), C^{4A}OOH cofactor (orange), substrate, and protein backbone (gray) over 400 ns MD simulations for the DszC:DPS (**a**) and DszC:DBT (**b**). (**c**,**d**) Radial distribution functions (g(r)) of water oxygen around the distal oxygen atom (O_d, orange) the proximal oxygen atom O_p(green)) and the sulfur atom (S,blue) of DPS in the DszC:DPS complex (**c**) and DszC:DBT complex (**d**).

The DPS is located within the catalytic pocket during the whole trajectory of 400 ns with a maximum RMSD at 4.7 Å and an averaged value of 3.19 Å (Figure 3a). The catalytic pocket is delimited by the active site (the co-factor C^{4a}OOH and the key residues around it as described above) and by a hydrophobic domain which comprises three phenylalanine and two tryptophan residues (Figure 2). This pocket is large

enough to accommodate easily the substrate DPS and even to let it drift away from the O_d atom of $C^{4a}OOH$ as shown by the fluctuations of the S–O_d distance between 3 Å and 8 Å (Figure S10). Those fluctuations are correlated with the dynamics of water molecules within the pocket. The RMSD of DPS remains stable near 2 Å during the first 50 ns, a period characterized by the complete absence of water molecules near the O_d atom. After 50 ns, some water molecules are located close to O_d while the RMSD of DPS increases to ~4 Å and the S–O_d distance increases to nearly 8 Å. At such position, the DPS substrate mostly interacts with the hydrophobic part of the catalytic pocket. By 140 ns, the hydration shell around O_d reached a steady state, with one or two water molecules within the first peak of the radial distribution function (Figure 3b,3c). Simultaneously, the RMSD of DPS stabilized around 3 Å and the S–O_d distance reaches a stable average of 3.5 Å (Figure 3a).

The presence of water in close contact with the active site contradicts the previous findings about the DszC:DBT case [25]. To check if this discrepancy is due to the substrate or to the quality of the sampling, we repeated the same analysis using DBT as a substrate and a long trajectory of 400 ns. As shown in Figure 2c, S8-S9, the behavior of the DszC:DBT complex is similar to the one of the DszC:DPS complex. The substrate drifts towards the hydrophobic part of the active site, with jumps in the RMSD of the substrate (RMSD around 5Å), a S-O_d distance that fluctuates between 3 Å and 12 Å (Figure S10), and one to two water molecules in close proximity to O_d (Figure S11). These water molecules were not present in the previous computational study [25], so their impact have not been yet reported. Their presence in the active site in DszC:DPS and DszC:DBT simulations indicates that this event is substrate-independent. In both cases, water molecules mostly interact with O_d-H group (Figure 3c,d). The analysis of the corresponding radial distribution functions suggests that in DszC:DBT case, the surrounding water molecule are more mobile and the interaction with O_d-H group less present than in the DszC:DPS case. This correlates with the higher mobility of DBT in the active site in our simulations: as the substrate comes closer to the hydrophilic pocket, more space can be explored by water molecules around O_d-H group. This different behavior can be due to conformational sampling issues. Overall, we can conclude that the presence of water molecule in the active site must not be neglected in the exploration of the catalytic mechanism of sulfoxidation in DszC.

4. Selection of Reactive Conformations of DPS for Sulfoxidation

Building upon the dynamic profiles and hydration patterns described above, we sought to identify several binding modes of DPS within the DszC active site. We base our selection on two key geometric parameters identified in DBT oxidation as key to enable low-energy-barrier pathways [25], the S–O_d distance and the S–O_d–O_p angle. Over the 400 ns MD trajectory, DPS predominantly sampled conformations with S–O_d distances between 2.5 – 4.5 Å and S–O_d–O_p angles of 130° – 170°, closely matching previously established optimal values for nucleophilic attack (S–O_d < 3.8 Å; angle > 146°) (Figure 4a). Applying these geometric criteria, we pre-selected 817 conformations for DPS.

To refine our selection, we identified other geometric parameters. A careful analysis of the trajectory revealed that two residues in close interaction with the C^{4a}OOH co-factor were exhibiting a dynamic behavior. First, we observed that the rotation of His391 allows this residue to serves as a hydrogen-bond acceptor ($O_dH\cdots N_\varepsilon$ < 2.2 Å) between 70–120 ns, while outside this window, it predominantly acts as a donor ($N_\delta H\cdots O_p$) (Figure 4b). Meanwhile, Tyr96 phenol group mainly functions as a hydrogen-bond donor ($O_\eta H\cdots O_p$) throughout the 400 ns simulation. However, occasional rotation of the OOH group also allows Tyr96 to act as an acceptor ($O_dH\cdots O_\eta$), when the intramolecular hydrogen bond is broken (Figure 4c). Besides, the possible presence of an intramolecular H-bond within the C^{4a}OOH co-factor is assessed in 82% of the selected conformations.

To further identify possible reactive conformations of the active site of DszC in presence of DPS, we then introduced a categorization scheme based on the h-bond network around the –OOH moiety of the C^{4a}OOH co-factor (Figure S13). We focused on the interaction of –OOH with His391 and Tyr96. This analysis identified three distinct families (**M1**–**M3**). The **M1** family is defined by the presence of an intramolecular H-bond within the C^{4a}OOH ($O_dH\cdots O2'$) while this bond is absent in the **M2** and **M3** families. The **M1** family is the largest, representing 82% of the population selected based on the S-O_d distance and the S-O_d-O_p angle (see above). We selected a representative conformation of M1 which maximizes the number of hydrogen bonds to stabilize the –OOH moiety, with His391 and Tyr96 serving as a H-bond donor. This conformation is schematically represented in Figure 5a. The **M2** family (12%

population) is characterized by His391 acting as a H-bond acceptor instead of a H-donor thanks to a rotation of this residue, and Tyr96 as a H-bond donor. The chosen representative structure is represented in Figure 5b. This structure closely resembles the reactive conformation for DBT previously reported by Fernandes *et a*l [25]. Finally, the **M3** family is defined by a rotation of the hydroxyl group of the -OOH moiety, with the OH group pointing towards Tyr96. Upon relaxing the S-O_d-O_p angle threshold to > 130° (while maintaining S–O_d < 3.8 Å), two candidate conformations were identified (Figure S14). In the selected conformation, Tyr96 acts as a H-bond acceptor and His391 acting as a H-bond donor, see Figure 5c.

To comprehensively assess the implications of the presence of water molecules within the active site (Figure 3c), we next sought to determine whether water molecules could participate to the stabilization of the –OOH group of the C^{4a}OOH co-factor, the O_p transfer to the S atom and the proton transfer from O_p to O_d. Specifically, we selected conformations in which a water molecule is h-bonded to the OOH group. Within the **M1** family, we selected one case: **M1-H_2O** retains the core hydrogen-bonding architecture of M1 but incorporates a water molecule that is H-bonded to O_dH ($O_dH\cdots O_w$ = 2.27 Å, see Figure 5d). In the frames corresponding to the **M2** family, no water molecules forms a hydrogen bond with the -OOH moiety. The **M3-H_2O** motif similarly extends the M3 architecture by incorporating a water molecule is H-bonded to O_dH ($O_w\cdots HO_d$, 1.84 Å, see Figure 5e).

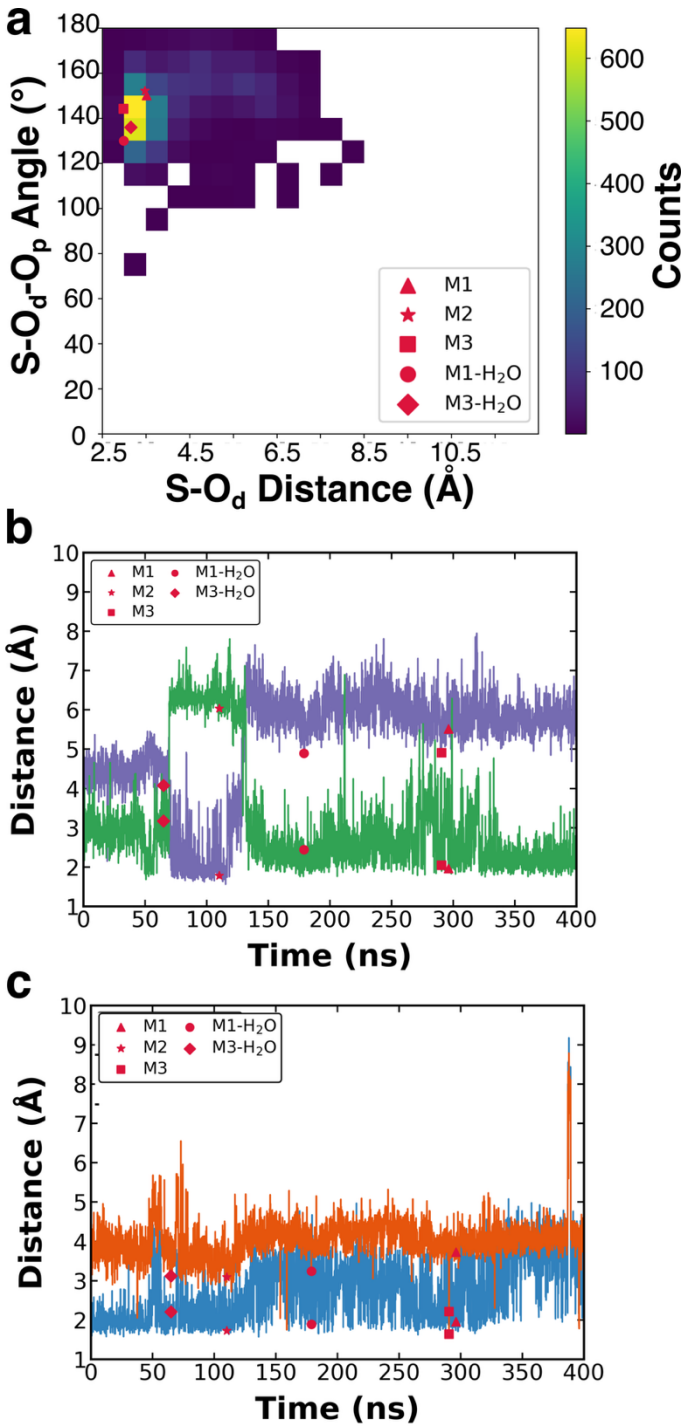

Figure 4. (a) two-dimensional histograms of S–O_d distance versus S–O_d–O_p angle for DszC:DPS during molecular dynamics (MD) simulations, where color-coded counts indicate conformational state frequencies; (b) time evolution of hydrogen-bond distances between O_dH of and N_ε of His391 (purple) and O_p and HN_δ of His391 (green) ; (c) time evolution of hydrogen-bond distances between O_dH of and O_η of Tyr96 (orange) and O_p and HO_η of Tyr96 (blue). The values of these geometrical parameters in the 5 selected starting points for QM/MM calculations are indicated with red symbols.

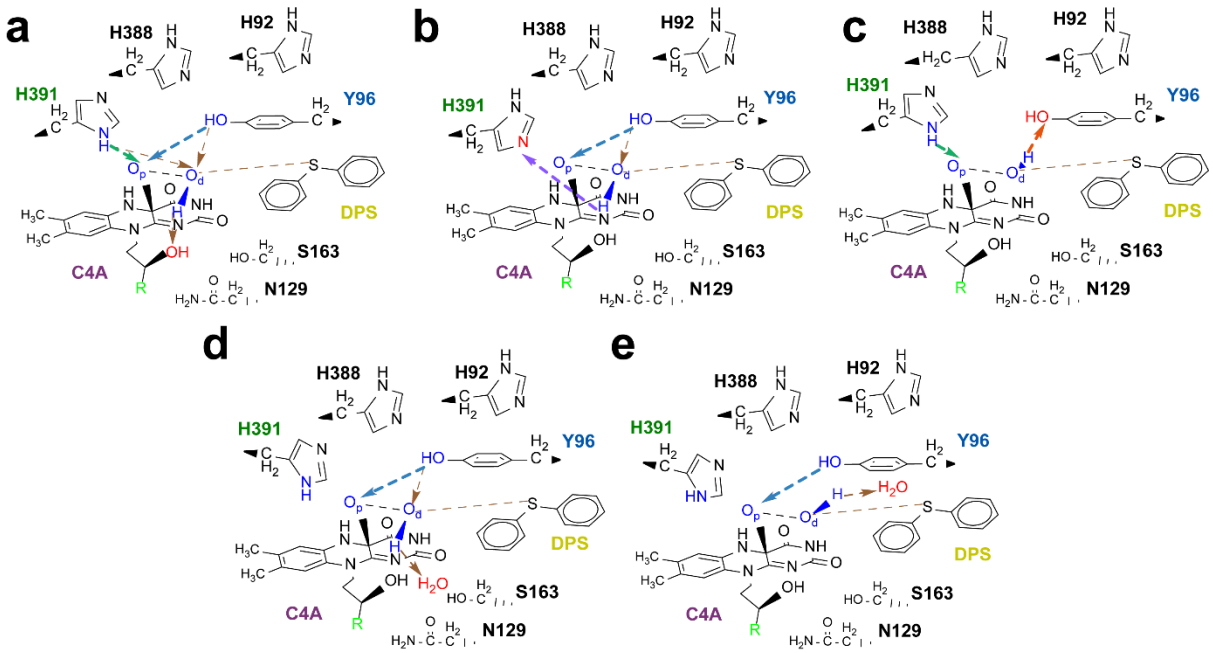

Figure 5. Representative active-site conformations for reactants selection M1 (**a**), M2 (**b**), M3 (**c**), M1-H_2O (**d**), and M3-H_2O (**e**), depicting distinct hydrogen-bonding networks.

5. Catalytic Mechanism of DPS Oxidation

To evaluate the activation barrier of the oxidation process catalyzed by DszC, we then moved to hybrid QM/MM calculations combined with geometry optimization and the NEB approach to optimize the path and then the transition state. The high flexibility of the active site is sampled thanks to the selection of three representative configurations (**M1**, **M2**, **M3**) from the long classical trajectory of 400ns. We also included a water molecule in the QM region in two cases (**M1-H_2O** and **M3-H_2O**). The resulting free energy profiles are provided in Figure 6a. This strategy is chosen as a good compromised between cost and accuracy and assumes that the dynamics of the enzymatic environment will stay frozen along the considered reaction pathways [51]. The alternative approach that consists in QM/MM biased dynamics simulations would require long trajectories along the reaction pathway to catch the rearrangement of the active site (e.g. rotation of His391) but also to avoid hysteresis issues [52].

After QM/MM geometry optimization, four models (**M1**, **M2**, **M3**, **M3-H_2O**) retained structural fidelity to MD predictions (Tables SX1–SX5). **M1-H_2O** underwent moderate polarization-induced rearrangement with a change of the directionality of the H-bond with the water molecule: after QM/MM optimization, O_d becomes a hydrogen bond acceptor for the water hydrogen. For each pathway, the reaction is exothermic with a $\Delta G°$ ranging from -31.8 kcal·mol^{-1} to -47.5 kcal·mol^{-1}. The optimized structures

of the reactant and product can be found in Figure S15, TS structures for M2, M3, M1-H_2O and M3-H_2O in Figure S16. Detailed structural information is collected in Table S1-S5.

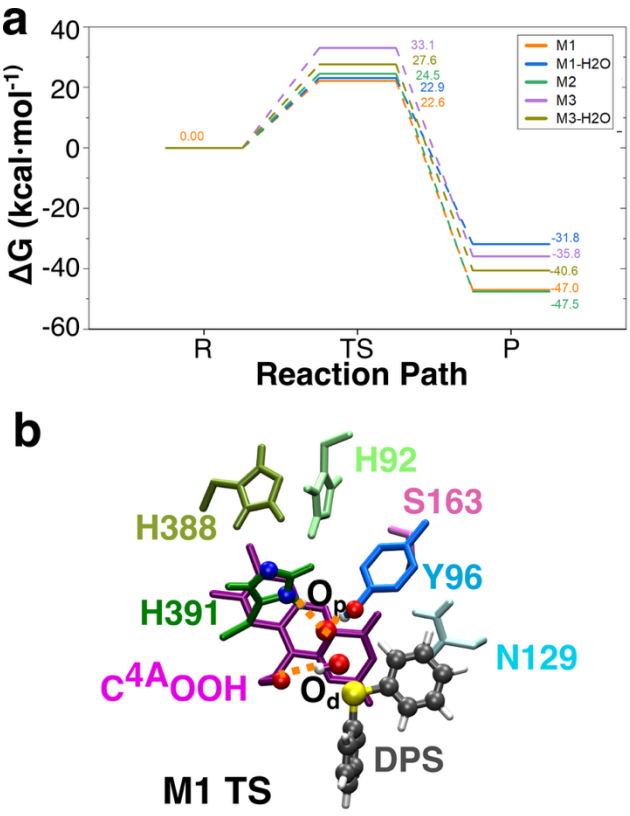

Figure 6. Free Energy Landscapes and Transition State Structure for DPS Oxidation Pathways. (a) Free energy profiles of DPS oxidation through five pathways (M1, M1-H_2O, M2, M3, M3-H_2O), with energy values in kcal·mol^{-1}. (b) Transition state (TS) structure for M1 pathway, highlighting hydrogen bonds around O_pO_dH group (orange dot lines).

The conformation of the active site has a strong influence on the activation free energy ($\Delta G^{\ddagger}$). During the O_d transfer, the proton of the –OOH moiety needs to be transferred to O_p, a process that can be assisted by the surrounding H-bond network. Despite similar starting S–O_d distance and S–O_d–O_p angle, we observe a gap of more than 10 kcal·mol^{-1} between the activation energies. The lowest activation energy (22.6 kcal·mol^{-1}) is obtained for **M1**, where the proton transfer from O_d to O_p is assisted by the intramolecular H-bond within the C^{4a}OOH co-factor ($O_{2'}\cdots HO_d$ = 2.11 Å in TS-M1) (Figure 6). In **M2**, the intramolecular H-bond is replaced by the His391 that was rotated to act as a H-bond acceptor ($N_\varepsilon\cdots HO_d$ = 1.57 Å in TS-M2), yielding to a slightly higher

barrier of 24.5 kcal·mol^{-1} (Figure S17). The highest barrier (33.1 kcal·mol^{-1}) is found in the **M3** case where Tyr96 assists the proton transfer ($O_\eta \cdots HO_d$ =1.81 Å in TS-M2). In all three cases the H-bond network around the -OOH moiety is maintained from the reactant to the transition state. In most cases, the H-bond distances vary by less than 0.2 Å in absolute value between the reactant and the TS. The only exceptions are found in **M1**. While the $O_2 \cdots HO_d$ is stirred from 1.69 Å to 2.11 Å, the $O_\eta H \cdots O_p$ is compressed from 1.83 Å to 1.58 Å. Hence, the most stabilizing interaction appears to be brought by the Tyr96 residue through H-bond donation to O_p. This interaction may be at the origin of the low barrier found in the **M1** case. Its absence in the **M3** case, where Tyr96 assists the proton transfer and hence cannot stabilize O_p during the O-O scission, is also likely at the origin of the high barrier obtained in this case.

The inclusion of water in the QM zone does not change the overall picture. The barriers are within the range obtained without including any water in the QM zone. In **M1-H_2O**, the barrier is slightly higher than in **M1** (22.9 kcal.mol^{-1} vs 22.6 kcal·mol^{-1}). In the transition state, the intramolecular H-bond within C^{4a}OOH assists the H-transfer in both cases and the extra water molecule only weakly interact with O_d moiety in TS-**M1-H_2O** ($H_w \cdots O_d$ = 2.19 Å). In **M3-H_2O**, His391 blocks the intramolecular H-bond within the C^{4a}OOH co-factor. The H-transfer is assisted by the added water ($O_w \cdots HO_d$ = 1.79 Å in TS-**M3-H_2O**). Nevertheless, the activation barrier is high (27.6 kcal·mol^{-1}). In both cases the stabilization of O_p by the Tyr96 residue relies on a weaker H-bond than in **M1** (1.76 Å in **M1-H_2O**, 1.83 Å in **M3-H_2O** vs. 1.58 Å in **TS-M1** and 1.89 Å in **M1**).

In short, the presence of water does not facilitate the oxidation of DPS. The H-transfer can be efficiently assisted by the intramolecular H-bond within the C^{4a}OOH co-factor. This conformation allows His391 and more importantly Tyr96 to stabilize the O_p atom through dative H-bonds during the O_p-O_d scission. Besides, the barriers values mirror the conformational frequency during MD simulations: M1, the most frequent conformation of the active site during MD simulation corresponds to the best starting geometry for enzymatic catalysis. This observation agrees the idea that the enzymatic active site favours the conformation closest to a transition state lower in energy.

6. Conclusion

Our combination of MD simulations and QM/MM calculations allow us to draw a catalytic mechanism for DPS sulfoxidation by DszC. This enzymatic reaction consists in the first step of C-S bond breaking by biomolecules, paving the way to a possible biodegradation of PPS polymer. Thanks to a filttering strategy along our MD trajectories, we are able to identify five potentially reactive conformations, highlighting the dynamical behavior of the active site. These conformations share a efficient reactive geometry of the sulfur atom of the substrate towards the –OOH group of the C^{4A}OOH cofactor, but differ by their hydrogen-bond network within the active site. The most frequent one conformation, involving hydrogen bonds between the O_p atom of C^{4A}OOH and His391 and Tyr96 residues and an intramolecular hydrogen bond within the C^{4A}OOH cofactor, also gives the lowest activation energy from our QM/MM calculation. This barrier is about 3 kcal·mol^{-1} higher than the one previously obtained for DBT,[25] so in line with biologically relevant mechanism. Moreover, our study highlights the crucial role played by Tyr96, which mutation can strongly impact the enzymatic activity towards DBT.[33,53] Taken together, our results provide a first approach for the design of processes for the biodegradation of PPS.

Acknowledgements

SSM acknowledges support by the "Initiative d'Excellence" program from the French State (Grants "DYNAMO", ANR-11-LABX-0011). PW gratefully acknowledges the support of K.C. Wong Education Foundation and Syensqo. We gratefully acknowledge support from the CBPsmn (PSMN, Pôle Scientifique de Modélisation Numérique) of the ENS de Lyon for the computing resources. The platform operates the SIDUS solution (https://dl.acm.org/doi/abs/10.5555/2555789.2555792) developed by Emmanuel Quemener.

References

1. Hill Jr., H.W.; Brady, D.G. Properties, environmental stability, and molding characteristics of polyphenylene sulfide. *Polym. Eng. Sci.* **1976**, *16* (12), 831–835.
2. Cleary, J.W. Poly(Phenylene Sulfide). In *Advances in Polymer Synthesis*; Culbertson, B.M., McGrath, J.E., Eds.; Springer: Boston, MA, 1985; pp 173–185.
3. Romero, N.A.; Parker, W.O.; Swager, T.M. Functional, Redox-Responsive Poly(phenylene sulfide)-Based Gels. *Macromolecules* **2019**, *52* (21), 8256–8265.
4. Zuo, P.; Tcharkhtchi, A.; Shirinbayan, M.; Fitoussi, J.; Bakir, F. Overall Investigation of Poly(Phenylene Sulfide) from Synthesis and Process to Applications—A Review. *Macromol. Mater. Eng.* **2019**, *304* (5), 1800686.
5. Gao, Y.; Zhou, X.; Zhang, M.; Lyu, L.; Li, Z. Polyphenylene Sulfide-Based Membranes: Recent Progress and Future Perspectives. *Membranes* **2022**, *12* (10), 924.

6. Shen, L.; Xing, J. The history, interests and future of polyphenylene sulfide: A bibliometric analysis. *High Perform. Polym.* **2023**, *36*, 36.
7. Phagare, M. *Polyphenylene Sulfide Market Report 2025 (Global Edition)*; Cognitive Market Research, 2025. Available online: https://www.cognitivemarketresearch.com/polyphenylene-sulfide-market-report
8. Okubo, K.; Sugeno, T.; Tagaya, H. Chemical recycling of poly(p-phenylene sulfide) in high temperature fluids. *Polym. Degrad. Stab.* **2015**, *111*, 109–113.
9. Yan, P.; Peng, W.; Yang, F.; Cao, Y.; Xiang, M.; Wu, T.; Fu, Q. Investigation on thermal degradation mechanism of poly(phenylene sulfide). *Polym. Degrad. Stab.* **2022**, *197*, 109863.
10. Ali, S.S.; Elsamahy, T.; Al-Tohamy, R.; Zhu, D.; Mahmoud, Y.A.G.; Koutra, E.; et al. Plastic wastes biodegradation: Mechanisms, challenges and future prospects. *Sci. Total Environ.* **2021**, *780*, 146590.
11. Tamoor, M.; Samak, N.A.; Jia, Y.; Mushtaq, M.U.; Sher, H.; Bibi, M.; et al. Potential Use of Microbial Enzymes for the Conversion of Plastic Waste Into Value-Added Products: A Viable Solution. *Front. Microbiol.* **2021**, *12*, 777420.
12. Zrimec, J.; Kokina, M.; Jonasson, S.; Zorrilla, F.; Zelezniak, A. Plastic-Degrading Potential across the Global Microbiome Correlates with Recent Pollution Trends. *mBio* **2021**, *12* (5), e02155-21.
13. Adomako, M.O.; Yu, F.-H. Potential effects of micro- and nanoplastics on phyllosphere microorganisms and their evolutionary and ecological responses. *Sci. Total Environ.* **2023**, *884*, 163760.
14. Golmohammadi, M.; Fatemeh Musavi, S.; Habibi, M.; Maleki, R.; Golgoli, M.; Zargar, M.; et al. Molecular mechanisms of microplastics degradation: A review. *Sep. Purif. Technol.* **2023**, *309*, 122906.
15. He, W.; Liu, S.; Zhang, W.; Yi, K.; Zhang, C.; Pang, H.; et al. Recent advances on microplastic aging: Identification, mechanism, influence factors, and additives release. *Sci. Total Environ.* **2023**, *889*, 164035.
16. Akram, J.; Hussain, M.U.; Aslam, A.; Akhtar, K.; Anwar, M.A.; Iqbal, M.; Hussain, M.T.; Akhtar, N. Genomic analysis and biodesulfurization potential of a new carbon–sulfur bond cleaving *Tsukamurella* sp. 3OW. *Int. Microbiol.* **2024**, *27* (5), 1429–1444.
17. Ahmad, A.; Zamzami, M.A.; Ahmad, V.; Al-Thawadi, S.; Akhtar, M.S.; Khan, M.J. Bacterial Biological Factories Intended for the Desulfurization of Petroleum Products in Refineries. *Fermentation* **2023**, *9* (3), 211.
18. Li, L.; Liao, Y.; Luo, Y.; Zhang, G.; Liao, X.; Zhang, W.; Zheng, S.; Han, S.; Lin, Y.; Liang, S. Improved Efficiency of the Desulfurization of Oil Sulfur Compounds in *Escherichia coli* Using a Combination of Desensitization Engineering and DszC Overexpression. *ACS Synth. Biol.* **2019**, *8* (6), 1441–1451.
19. Li, J.; Kim, H.R.; Lee, H.M.; Yu, H.C.; Jeon, E.; Lee, S.; Kim, D.-H. Rapid biodegradation of polyphenylene sulfide plastic beads by *Pseudomonas* sp. *Sci. Total Environ.* **2020**, *720*, 137616.
20. Lee, H.M.; Kim, H.R.; Jeon, E.; Yu, H.C.; Lee, S.; Li, J.; Kim, D.-H. Evaluation of the Biodegradation Efficiency of Four Various Types of Plastics by *Pseudomonas aeruginosa* Isolated from the Gut Extract of Superworms. *Microorganisms* **2020**, *8* (9), 1341.
21. Ahmad, M.; Yousaf, M.; Han, J.-C.; Ur Rahman, S.; Muhammad Adeel Sharif, H.; Wang, L.; Tang, Z.; Zhou, Y.; Huang, Y. State-of-the-art analysis of the fuel desulphurization processes: Perspective of CO_2 utilization in coal biodesulphurization. *Chem. Eng. J.* **2023**, *478*, 147517.
22. Caro, A.; Boltes, K.; Letón, P.; García-Calvo, E. Dibenzothiophene biodesulfurization in resting cell conditions by aerobic bacteria. *Biochem. Eng. J.* **2007**, *35* (2), 191–197.
23. Sousa, J.P.M.; Ferreira, P.; Neves, R.P.P.; Ramos, M.J.; Fernandes, P.A. The bacterial 4S pathway – an economical alternative for crude oil desulphurization that reduces CO_2 emissions. *Green Chem.* **2020**, *22* (22), 7604–7621.
24. Bhanjadeo, M.M.; Rath, K.; Gupta, D.; Pradhan, N.; Biswal, S.K.; Mishra, B.K.; Subudhi, U. Differential desulfurization of dibenzothiophene by newly identified MTCC strains: Influence of Operon Array. *PLoS ONE* **2018**, *13* (3), e0192536.
25. Barbosa, A.C.C.; Neves, R.P.P.; Sousa, S.F.; Ramos, M.J.; Fernandes, P.A. Mechanistic Studies of a Flavin Monooxygenase: Sulfur Oxidation of Dibenzothiophenes by DszC. *ACS Catal.* **2018**, *8* (10), 9298–9311.
26. Neves, R.P.P.; Ramos, M.J.; Fernandes, P.A. Engineering DszC Mutants from Transition State Macrodipole Considerations and Evolutionary Sequence Analysis. *J. Chem. Inf. Model.* **2023**, *63* (1), 20–26. DOI: 10.1021/acs.jcim.2c01337.

27. Ferreira, P.; Neves, R.P.P.; Miranda, F.P.; Cunha, A.V.; Havenith, R.W.A.; Ramos, M.J.; Fernandes, P.A. DszA Catalyzes C–S Bond Cleavage through N5–Hydroperoxyl Formation. *J. Chem. Inf. Model.* **2024**, *64* (10), 4218–4230.
28. Sousa, J.P.M.; Neves, R.P.P.; Sousa, S.F.; Ramos, M.J.; Fernandes, P.A. Reaction Mechanism and Determinants for Efficient Catalysis by DszB, a Key Enzyme for Crude Oil Bio-desulfurization. *ACS Catal.* **2020**, *10* (16), 9545–9554.
29. Sousa, S.F.; Sousa, J.F.M.; Barbosa, A.C.C.; Ferreira, C.E.; Neves, R.P.P.; Ribeiro, A.J.M.; Fernandes, P.A.; Ramos, M.J. Improving the Biodesulfurization of Crude Oil and Derivatives: A QM/MM Investigation of the Catalytic Mechanism of NADH-FMN Oxidoreductase (DszD). *J. Phys. Chem. A* **2016**, *120* (27), 5300–5306.
30. Abin-Fuentes, A.; Mohamed Magdy, E.-S.; Wang, D.I.C.; Prather, K.L.J. Exploring the Mechanism of Biocatalyst Inhibition in Microbial Desulfurization. *Appl. Environ. Microbiol.* **2013**, *79* (24), 7807–7817.
31. Raheb, J.; Naghdi, S.; Karkhane, A.A.; Yakhchali, B.; Flint, K. Designing a new recombinant strain with additional copy number of *dsz* cluster to enhance biodesulfurization activity in *Pseudomonas aeruginosa* ATCC 9027. *Iran. J. Sci. Technol. Trans. A: Sci.* **2005**, *29* (1), 195–199. DOI: 10.22099/ijsts.2005.2797.
32. Callender, R.; Dyer, R.B. The Dynamical Nature of Enzymatic Catalysis. *Acc. Chem. Res.* **2015**, *48* (2), 407–413. DOI: 10.1021/ar5002928.
33. Liu, S.; Zhang, C.; Su, T.; Wei, T.; Zhu, D.; Wang, K.; Huang, Y.; Dong, Y.; Yin, K.; Xu, S.; Xu, P.; Gu, L. Crystal structure of DszC from *Rhodococcus* sp. XP at 1.79 Å. *Proteins: Struct., Funct., Bioinf.* **2014**, *82* (9), 1708–1720.
34. Alfieri, A.; Fersini, F.; Ruangchan, N.; Prongjit, M.; Chaiyen, P.; Mattevi, A. Structure of the monooxygenase component of a two-component flavoprotein monooxygenase. *Proc. Natl. Acad. Sci. U.S.A.* **2007**, *104* (4), 1177–1182.
35. Schrödinger, LLC. *The PyMOL Molecular Graphics System*, Version 3.1; Schrödinger, LLC: New York, NY, 2015.
36. Case, D.A.; Cheatham III, T.E.; Darden, T.; Gohlke, H.; Luo, R.; Merz Jr., K.M.; Onufriev, A.; Simmerling, C.; Wang, B.; Woods, R.J. The Amber biomolecular simulation programs. *J. Comput. Chem.* **2005**, *26* (16), 1668–1688.
37. Götz, A.W.; Williamson, M.J.; Xu, D.; Poole, D.; Le Grand, S.; Walker, R.C. Routine Microsecond Molecular Dynamics Simulations with AMBER on GPUs. 1. Generalized Born. *J. Chem. Theory Comput.* **2012**, *8* (5), 1542–1555.
38. Maier, J.A.; Martinez, C.; Kasavajhala, K.; Wickstrom, L.; Hauser, K.E.; Simmerling, C. ff14SB: Improving the Accuracy of Protein Side Chain and Backbone Parameters from ff99SB. *J. Chem. Theory Comput.* **2015**, *11* (8), 3696–3713.
39. TURBOMOLE V7.5.1 2021, a development of University of Karlsruhe and Forschungszentrum Karlsruhe GmbH, 1989-2007, TURBOMOLE GmbH, since 2007; available from https://www.turbomole.org.
40. Franzke, Y.J.; Holzer, C.; Andersen, J.H.; Begušić, T.; Bruder, F.; Coriani, S.; Della Sala, F.; Fabiano, E.; Fedotov, D.A.; Fürst, S.; et al. TURBOMOLE: Today and Tomorrow. *J. Chem. Theory Comput.* **2023**, *19* (20), 6859–6890. DOI: 10.1021/acs.jctc.3c00347.
41. Jorgensen, W.L.; Chandrasekhar, J.; Madura, J.D.; Impey, R.W.; Klein, M.L. Comparison of simple potential functions for simulating liquid water. *J. Chem. Phys.* **1983**, *79* (2), 926–935.
42. Roe, D.R.; Cheatham, T.E. III. PTRAJ and CPPTRAJ: Software for Processing and Analysis of Molecular Dynamics Trajectory Data. *J. Chem. Theory Comput.* **2013**, *9* (7), 3084–3095. DOI: 10.1021/ct400341p.
43. Neese, F. The ORCA program system. *WIREs Comput. Mol. Sci.* **2012**, *2* (1), 73–78.
44. Neese, F. Software update: The ORCA program system—Version 5.0. *WIREs Comput. Mol. Sci.* **2022**, *12* (5), e1606.
45. Ásgeirsson, V.; Birgisson, B.O.; Bjornsson, R.; Becker, U.; Neese, F.; Riplinger, C.; Jónsson, H. Nudged Elastic Band Method for Molecular Reactions Using Energy-Weighted Springs Combined with Eigenvector Following. *J. Chem. Theory Comput.* **2021**, *17* (8), 4929–4945.
46. Baker, J. An algorithm for the location of transition states. *J. Comput. Chem.* **1986**, *7* (4), 385–395.
47. Humphrey, W.; Dalke, A.; Schulten, K. VMD: Visual molecular dynamics. *J. Mol. Graph.* **1996**, *14*, 33–38.
48. Visitsatthawong, S.; Chenprakhon, P.; Chaiyen, P.; Surawatanawong, P. Mechanism of Oxygen Activation in a Flavin-Dependent Monooxygenase: A Nearly Barrierless Formation of

C4a-Hydroperoxyflavin via Proton-Coupled Electron Transfer. *J. Am. Chem. Soc.* **2015**, *137* (29), 9363–9374.
49. Zhang, Q.; Wang, B. Mechanistic Perspective on Oxygen Activation Chemistry by Flavoenzymes. *ChemBioChem* **2025**, *26* (2), e202400750.
50. Neves, R.P.P.; Araújo, B.; Ramos, M.J.; Fernandes, P.A. Feedback Inhibition of DszC, a Crucial Enzyme for Crude Oil Biodessulfurization. *Catalysts* **2023**, *13* (4), 736.
51. Cerqueira, N.M.F.S.A.; Fernandes, P.A.; Ramos, M.J. Protocol for Computational Enzymatic Reactivity Based on Geometry Optimisation. *ChemPhysChem* **2018**, *19* (6), 669–689. DOI: 10.1002/cphc.201700339.
52. Świderek, K.; Tuñón, I.; Moliner, V. Predicting enzymatic reactivity: from theory to design. *WIREs Comput. Mol. Sci.* **2014**, *4* (5), 407–421. DOI: 10.1002/wcms.1173.
53. Zhang, L.; Duan, X.; Zhou, D.; Dong, Z.; Ji, K.; Meng, W.; Li, G.; Li, X.; Yang, H.; Ma, T.; et al. Structural insights into the stabilization of active, tetrameric DszC by its C-terminus. *Proteins: Struct., Funct., Bioinf.* **2014**, *82* (10), 2733–2743. DOI: 10.1002/prot.24638.